Lattice Boltzmann method simulation of ice melting process in the gas diffusion layer of fuel cell

Pu He [a], Li Chen [a], Yu-Tong Mu [b], Wen-Quan Tao [a],*

[a] *Key Laboratory of Thermo-Fluid Science and Engineering of MOE, School of Energy and Power Engineering, Xi'an Jiaotong University, Xi'an, Shaanxi 710049, China*
[b] *School of Human Settlements and Civil Engineering, Xi'an Jiaotong University, Xi'an, Shaanxi 710054, China*

ABSTRACT

A 2D lattice Boltzmann model combining the enthalpy-based method (EBM) is established to investigate the ice melting process in the gas diffusion layer (GDL). The effects of GDL melting position, porosity, Rayleigh number and Stefan number on the melting rate, ending time of melting, temperature distribution and solid-liquid interface distribution are investigated. It is found that the GDL melting positions have a significant effect on the melting process, the melting rate in the In-plane position increases fastest. When the porosity is large, the effect of the carbon fiber layer number on the melting process is more significant than that of the carbon fiber length. In the In-plane position, the increase of natural convection intensity has a promoting effect on the ice melting process. The increasing of Stefan number can promote the melting process significantly when the Stefan number is not high. And reducing the GDL porosity can effectively promote the melting process.

© 2019 Elsevier Ltd. All rights reserved.

1. Introduction

The melting process in porous media is pervasive in natural and industrial processes. Typical examples include the melting process in the phase change material (PCM) [1–4], and cold start in fuel cell [5–8].

Due to its excellent merits of energy storage ability in releasing and storing latent heat in a small range of temperatures, PCM has been widely used in aerospace, electronics cooling and building energy management [9–12]. However, PCM has an unavoidable disadvantage of low heat transfer rate because of its low thermal conductivity [2]. To improve the conductivity of PCM, nanoparticles with high thermal conductivity and metal foam are often added in PCM [13–15]. However, the addition of particles can reduce the effective volume of PCM, therefore, there exists an appropriate limit for the addition of particles to make full use of PCM. In order to find the optimum particle addition for different materials of PCM in different application situations, research work is highly needed.

A fuel cell is an energy conversion device that can convert the chemical energy stored in fuel to electronic energy directly. Among the different types of fuel cells, proton exchange membrane (PEM) fuel cell has attracted more and more attention due to its ad-

vantages of high power density, low operating temperature and low emission. However, for its application in auto, the PEM fuel cell must be operated in a wide range of environmental temperatures, ranging from about -30 °C to 70 °C. Within so wide temperature variation range and with the effects of electro-chemical reaction, the water and heat management of PEM fuel cell is very complicated, in which phase change, diffusion of gas species, action of capillary force and electro-osmotic drag, etc. Particularly, when the environmental temperature is below 0 °C, the water existing in the fuel cell is frozen, and this frozen water should be melted in a short time for a successful start-up of the PEM fuel cell (the so-called cold start process). The successful cold start of the PEM fuel cell is one of the key problems for the commercialization of the PEM fuel cell on auto in cold regions, and it has attracted much research attention. Following is a brief review of this aspect. Ahluwalia and Wang [16] developed a two-dimensional model to study the effect of feed gas temperatures, operating pressure, and electrical heating on the cold start performance. Meng [17] developed a transient multiphase multi-dimensional PEM fuel cell model to elucidate the fundamental physics of cold start. Jiao and Li [18] developed a three-dimensional multiphase model to simulate the process of cold start in PEM fuel cell. Guo et al. [19] studied an assisted cold start process for the PEM fuel cell by a three-dimensional multiphase model. Du et al. [20] developed a multiphase stack model to study the maximum power cold start mode of PEM fuel cell. In order to control the water content in

Nomenclature

c	velocity in lattice unit
C_p	heat capacity
c_s	sound speed in lattice unit
$\boldsymbol{e}_i$	discrete velocity in the ith direction
En	enthalpy
En_l	enthalpy of the liquid phase at the melting temperature
En_s	enthalpy of the solid phase at the melting temperature
$\boldsymbol{f}$	body force of the flow fluid
f_l	melting fraction
f_i	particle distribution for fluid flow in the ith direction
f_i^{eq}	equilibrium distribution function for fluid flow in the ith direction
Fo	Fourier number
F_i	body force term
$\boldsymbol{g}$	gravitational acceleration
g_i	particle distribution for heat transfer in the ith direction
g_i^{eq}	equilibrium distribution function for heat transfer in the ith direction
J_i	the rest fraction in Eq. (19)
L_f	latent heat of fusion
l_0	length scale
Pr	Prandtl number
Ra	Rayleigh number
St	Stefan number
t	time
t_0	time scale
T	temperature
w_i	weight factor in the ith direction
x_m	position of the solid-liquid interface

Greek letters

α	thermal diffusivity
α_L	thermal diffusivity in the lattice unit
α_P	thermal diffusivity in the physical unit
β	thermal expansion coefficient
λ	coefficient related to Stefan number
υ	kinematics viscosity
υ_L	kinematics viscosity in the lattice unit
υ_P	kinematics viscosity in the physical unit
τ_f	relaxation time related to the kinematics viscosity
τ_g	relaxation time related to the thermal diffusivity

the membrane electrode assembly of PEM fuel cell and to facilitate the cold start process, Mu et al. [21] studied the gas purge process and summarized the effects of operation conditions by a three-dimensional multiphase non-isothermal unsteady model. The above-mentioned numerical studies conducted on the cold start of PEM fuel cell are all based on the continuum assumption. Because the porous structure of gas diffusion layer (GDL) and catalyst layer (CL) in the PEM fuel cell are mesoscale in size, the study of melting process from the mesoscopic or microscopic point view is meaningful and helpful for deeply understanding the cold start process of the PEM fuel cell. However, to the authors' knowledge, so far no such numerical study has been published.

The lattice Boltzmann method (LBM) is based on the particle distribution equations which describe the mesoscopic characteristics of the computational particles and output the macroscopic parameters. Compared with the macroscopic method, LBM has several merits such as an excellent ability of parallel computing and

convenience of complex boundary operation. Due to the advantages mentioned above, LBM is very suited to study the physical processes within the mesoscale structure, and in [22–24] such applications were conducted for non-PEM fuel cell cases. In [25] a comprehensive review was made for the pseudopotential multiphase lattice Boltzmann model. Chen et al. [26] employed the LBM to investigate pore-scale flow and mass transport in the GDL in the fuel cell, and presented a detailed description of the pore-scale liquid water behaviors. In [27], an LBM model was established to study the electro-chemical reaction process in the catalyst layer of PEM fuel cell, and the effect of non-precious catalyst and Pt on the reactive surface area and catalyst reaction rate was studied. Chen et al. [28] used the LBM to study the oxygen transportation in a new construction of CL, which is consisted of carbon particle, ionomer, Pt particles and primary pores. Mu et al. [29] developed a mesoscopic model by the LBM to study the transport resistance of hydrogen in CL. For the study of melting process, Jiaung et al. [30] developed an extended lattice Boltzmann equation to simulate the phase change problem governed by the conduction process with two types of boundary conditions. Chatterjee and Chakraborty [31] developed a three-dimensional model by LBM to study the phase change process, in which the enthalpy-based approach was used to track the solid-liquid interface. Huber et al. [32] developed an LBM model coupled with thermal convection and melting, and analyzed the transition from conduction-dominated heat transfer to fully-developed convection in detail. Li et al. [33] coupled LBM with an interfacial tracking method to solve melting controlled by conduction and convection. Later they used LBM to develop a three-dimensional multiple-relaxation-time model to simulate the melting process controlled by convection [34]. All the above LBM studies about phase change processes are quite general, no one is directed to the melting process during the cold-start process of the fuel cell.

In this study, taking the cold-start of fuel cell as its engineering background, the melting process of ice in porous media is investigated, a two-dimensional LBM model for fluid flow coupled with a thermal LBM model based on enthalpy method (EBM) is developed, and the effects of GDL melting position, porosity, Rayleigh number and Stefan number on the melting rate, ending time of melting, temperature distribution and solid-liquid interface distribution are investigated. In the following the physical problem studied is first described in Section 2, followed by the numerical method in Section 3. Then in Section 4 results of the simulation for the ice melting process in the gas diffusion layer of the fuel cell will be presented and discussed in detail. Finally, some conclusions are drawn in Section 5.

2. Physical problem

The major focus of this paper is to investigate the melting process dominated by convection. However, for the validation of numerical methods, the problem of melting dominated by conduction (later conduction melting for simplicity) with homogeneous, isotropic thermal diffusivity is first studied which can be solved by analytical method. In the following, the conduction-dominated problem and the convection-dominated problem will be presented in order.

The physical problem and the boundary conditions for the conduction melting are shown in Fig. 1(a), and the heat transfer process can be described by the following equation [35]:

$$\frac{\partial T}{\partial t} = \alpha \nabla^2 T \tag{1}$$

where T, t and α are the temperature, time and thermal diffusivity respectively. According to the energy balance, the following equa-
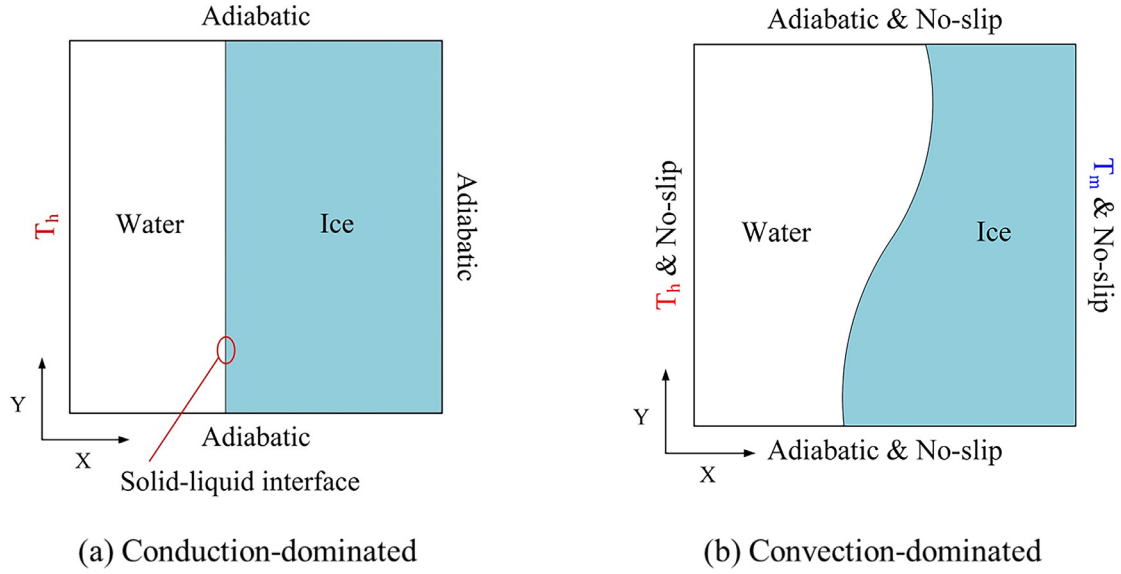
Fig. 1. Schematic of the melting process.

tion is satisfied on the solid-liquid interface [35]

$$\alpha\left(\frac{\partial T}{\partial x}\right)_{x=x_m} = \frac{L_f}{C_p}\frac{dx_m}{dt} \tag{2}$$

where L_f, C_p and x_m are the latent heat of fusion, heat capacity and position of the solid-liquid interface respectively.

When the initial temperature of a system is at the melting temperature, the analytical solution of Eq. (1) with the interface condition of Eq. (2) can be described as [35]

$$T(x,t) = T_h - (T_h - T_m)\frac{erf\left[x/(2\sqrt{\alpha t})\right]}{erf(\lambda)} \tag{3}$$

$$x_m(t) = 2\lambda\sqrt{\alpha t} \tag{4}$$

where λ is the coefficient determined by the following equation [35]

$$\lambda\exp(\lambda^2)erf(\lambda) = \frac{St}{\sqrt{\pi}} \tag{5a}$$

and St in Eq. (5a) is Stefan number defined by

$$St = \frac{C_p(T_h - T_m)}{L_f} \tag{5b}$$

The analytical solution of the conduction melting problem shown above will be served as the reference one for the validation of numerical methods.

The problem of melting in cavity dominated by natural convection (later natural convection melting for simplicity) for incompressible Newtonian fluid is shown in Fig. 1(b). For this problem, the Boussinesq approximation is introduced, and the continuity equation, momentum conservation equation, energy conservation equation can be written respectively as [36]

$$\nabla \cdot \mathbf{u}^* = 0 \tag{6}$$

$$\frac{\partial \mathbf{u}^*}{\partial t} + \mathbf{u}^* \cdot (\nabla \mathbf{u}^*) = -\nabla p^* + Pr\nabla^2\mathbf{u}^* - PrRa\beta T^* \tag{7}$$

$$\frac{\partial T^*}{\partial t^*} + \mathbf{u}^* \cdot \nabla T^* = \nabla^2 T^* - \frac{1}{St}\frac{\partial f_l}{\partial t^*} \tag{8}$$

where $Pr = \upsilon/\alpha$ is Prandtl number, $Ra = g\beta\Delta TH^3/(\alpha\upsilon)$ is Rayleigh number and f_l is the melting fraction. The parameters of υ, g and β are kinematics viscosity, gravitational acceleration and thermal expansion coefficient respectively. The boundary conditions

are shown in Fig. 1(b) and will not be restated here for simplicity.

3. Numerical method

Due to the merits of easy boundary condition treatment between fluid and solid, and the great ability in parallel computation, LBM has been developed to be a very powerful tool to study the mass and heat transfer process in porous media during the past two decades. An introduction of the LBM model in this study is given in the following paragraphs.

3.1. LBM for fluid flow

In this study, the Bhatnagar-Gross-Krook (BGK) method is employed to achieve flow velocity [37]. The evolution equation with the effect of buoyancy force for the particle distribution $f_i(x, t)$ is

$$f_i(x + \mathbf{e}_i\Delta t_1, t + \Delta t_1) - f_i(x, t) = -\frac{1}{\tau_f}\left[f_i(x,t) - f_i^{eq}(x,t)\right] + \Delta t_1 F_i \tag{9}$$

where Δt is the time increment, τ_f is the relaxation time related to the kinematics viscosity. $\mathbf{e}_i$ is the discrete velocity, and in D2Q9 used in this study, it is defined as

$$\mathbf{e}_i = \begin{cases} 0 & i = 0 \\ (\cos[(i-1)\pi/2], \sin[(i-1)\pi/2]) & i = 1,2,3,4 \\ \sqrt{2}(\cos[(2i-9)\pi/4], \sin[(2i-9)\pi/4]) & i = 5,6,7,8 \end{cases} \tag{10}$$

The equilibrium distribution function $f_i^{eq}(x, t)$ is calculated as

$$f_i^{eq}(x,t) = w_i\rho\left[1 + \frac{\mathbf{e}_i \cdot \mathbf{u}}{(c_s)^2} + \frac{(\mathbf{e}_i \cdot \mathbf{u})^2}{2(c_s)^4} - \frac{\mathbf{u} \cdot \mathbf{u}}{2(c_s)^2}\right] \tag{11}$$

where $c_s = c/\sqrt{3}$ is the sound speed in the lattice unit, and $c = \Delta x/\Delta t$ is the velocity in the lattice unit. w_i is the weight factor, and for D2Q9 model, it is defined as

$$w_i = \begin{cases} 4/9 & i = 0 \\ 1/9 & i = 1,2,3,4 \\ 1/36 & i = 5,6,7,8 \end{cases} \tag{12}$$

The body force term F_i is defined as

$$F_i = w_i\left(1 - \frac{1}{2\tau_v}\right)\left(\frac{\mathbf{e}_i - \mathbf{u}}{c_s^2} + \frac{\mathbf{e}_i \cdot \mathbf{u}}{c_s^4}\mathbf{e}_i\right) \cdot \boldsymbol{f} \tag{13}$$

where $\boldsymbol{f}$ is the body force of the flow fluid, and it can be calculated as

$$\boldsymbol{f} = \rho\mathbf{g}\beta(T - T_{\text{ref}}) \tag{14}$$

By means of Chapman-Enskog expansion, the macroscopic momentum equation, Eq. (7), can be derived from this model.

The macroscopic parameters such as density and velocity can be calculated respectively as

$$\rho = \sum_i f_i \tag{15}$$

$$\rho u = \sum_i f_i\mathbf{e}_i + \frac{\Delta t_1}{2}\mathbf{f} \tag{16}$$

The kinematics viscosity in lattice unit can be defined as

$$\upsilon_L = c_s^2\left(\tau_v - \frac{1}{2}\right)dt \tag{17}$$

where dt is the time step.

The kinematics viscosity in the physical unit can be achieved by

$$\upsilon_P = \upsilon_L\frac{l_0^2}{t_0} \tag{18}$$

where l_0 and t_0 are length scale and time scale respectively.

In the study of the melting process, there is an interface between fluid and solid. The interface treatment in LBM is shown in Fig. 2.

3.2. LBM for heat transfer

For the heat transfer in different fluid and solid area, the evolution equation $g_i(x, t)$ for the particle distribution can be defined as

$$g_i(x + \mathbf{e}_i\Delta t_2, t + \Delta t_2) - g_i(x, t) = -\frac{1}{\tau_g}\left[g_i(x, t) - g_i^{eq}(x, t)\right] \tag{19}$$

where τ_g is the relaxation time and $g_i^{eq}(x, t)$ is the equilibrium distribution function, which is calculated as

$$g_i^{eq}(x, t) = T\left(J_i + \frac{1}{2}\mathbf{e}_i \cdot \mathbf{u}\right) \tag{20}$$

where J_i is the rest fraction.

For the heat transfer, D2Q5 has enough accuracy to simulate the process [38], therefore, it is adopted to calculate the particle distribution, and the discrete velocity is defined as

$$\mathbf{e}_i = \begin{cases} 0 & i = 0 \\ (\cos[(i-1)\pi/2], \sin[(i-1)\pi/2]) & i = 1, 2, 3, 4 \end{cases} \tag{21}$$

The rest fraction J_i in Eq. (20) can be calculated as

$$J_i = \begin{cases} J_0 & i = 0 \\ (1 - J_0)/4 & i = 1, 2, 3, 4 \end{cases} \tag{22}$$

where the rest fraction J_0 can be chosen from 0 to 1 ($J_0 = 0.2$ in this simulation).

The temperature can be obtained by

$$T = \sum_i g_i \tag{23}$$

The thermal diffusivity in the lattice unit can be calculated as

$$\alpha_L = \frac{1}{2}(1 - J_0)\left(\tau_g - \frac{1}{2}\right)dt \tag{24}$$

The thermal diffusivity in the physical unit can be achieved by

$$\alpha_P = \alpha_L\frac{l_0^2}{t_0} \tag{25}$$

The kinematics viscosity in Eq. (17) and the thermal diffusivity in Eq. (24) are related to each other by Prandtl number:

$$Pr = \frac{\upsilon_L}{\alpha_L} \tag{26}$$

Substituting Eqs. (17) and (24) to Eq. (26), the following equation can be acquired:

$$Pr = \frac{2(\tau_v - 0.5)}{3(1 - J_0)(\tau_g - 0.5)} \tag{27}$$

3.3. Interface-track model

In this study, the enthalpy-based method (EBM) is employed to track the solid-liquid interface and the schematic for the interface-track model is shown in Fig. 2.

The local enthalpy can be calculated as

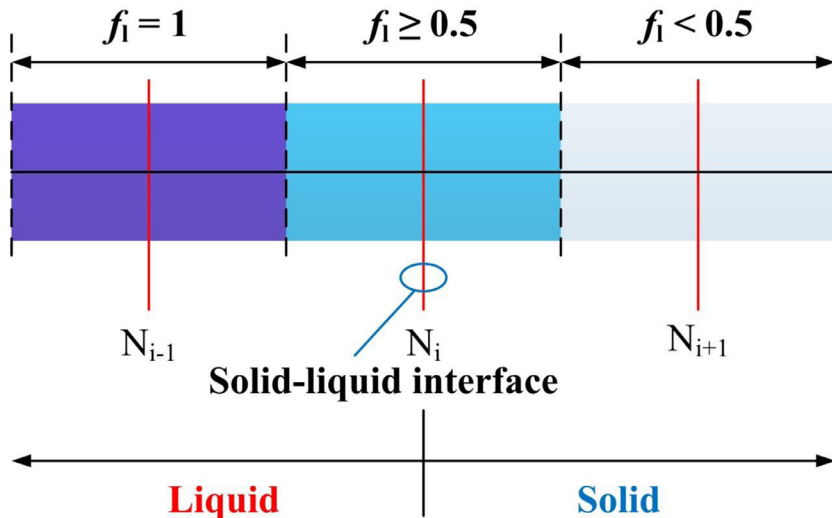$$En^k = c_pT^k + L_ff_l^{k-1} \tag{28}$$

Fig. 2. Schematic of the interface-track LB model.

where En^k and T^k are the local enthalpy and temperature for the present time step respectively, moreover, f_l^{k-1} is the liquid fraction for the previous time step, and it can be updated by Jiaung et al. [39]

$$f_l^k = \begin{cases} 0 & En^k < En_s = c_p T_m \\ \dfrac{En^k - En_s}{En_l - En_s} & En_s \le En^k \le En_l = En_s + L_f \\ 1 & En^k > En_l = En_s + L_f \end{cases} \quad (29)$$

By introducing enthalpy, the evolution equation of $g_i(x,t)$, Eq. (19), can be modified as

$$g_i(x + \mathbf{e}_i \Delta t, t + \Delta t) - g_i(x, t) = -\frac{1}{\tau_g}\left[g_i(x, t) - g_i^{eq}(x, t)\right]$$
$$-w_i \frac{L_f}{c_p}\left[f_l^k(x) - f_l^{k-1}(x)\right] \quad (30)$$

The macroscopic energy equation, Eq. (8), can be derived from Eq. (30) by Chapman-Enskog expansion.

In this study, for the convection melting process, when the liquid fraction computed in Eq. (29) is bigger than 0.5, the collision step in fluid flow model occurs, otherwise, the bounce back boundary for fluid flow is implemented, and the velocity is fixed as 0, which can ensure the coupling between fluid flow, heat transfer and phase change model. On the other hand, for the conduction melting, only heat transfer and the interface track models are solved, thus, the coupling between heat transfer and the interface track model is simpler than the convection melting process.

The porous media structure studied in this paper is consisted of carbon fibers and pores. The parameters of ice, water and carbon fiber used in this study are listed in Table 1. In this simulation, the

Table 1
Properties of water, ice and carbon fiber.

Substance	Parameter	Value
Water (273 K)	Heat capacity	$C_p = 4212$ J/(kg·K)
	Kinematics viscosity	$\upsilon_p = 1.789 \times 10^{-6}$ m^2/s
	Thermal diffusivity	$\alpha_p = 13.1 \times 10^{-8}$ m^2/s
	Prandtl number	$Pr = 13$
Ice	Latent heat of fusion	$L_f = 333550.0$ J/kg
	Thermal diffusivity	$\alpha_p = 12.4 \times 10^{-7}$ m^2/s
	Melting temperature	$T_m = 273$ K
Carbon fiber	Thermal diffusivity	$\alpha_p = 1.76 \times 10^{-6}$ m^2/s

kinematics viscosity in the lattice unit can be calculated as

$$\upsilon_L = \sqrt{\frac{g\beta(T_h - T_m)H^3 Pr}{Ra}} \quad (31)$$

where β is the thermal expansion coefficient.

In the simulation, because of the different thermal diffusivities of ice, water and carbon fibers, the different relaxation time defined in Eq. (24) is used in these three computational components.
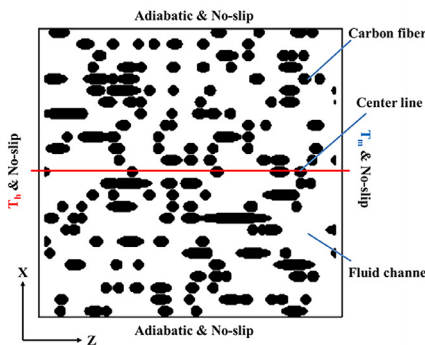
3.4. Computational domain

Fig. 1 schematically shows the computational domain and boundary condition for the conduction-dominated and convection-dominated melting process in the square cavity without a porous structure. The conduction melting is carried out in a cavity shown in Fig. 1(a) where the thermal boundary conditions are also indicated. Initially, the cavity is filled by solid ice at zero degree of Celsius, and with the heating at the left wall the ice solid gradually melted. Fig. 3 shows the computational domain for the convection melting in the porous structure of this study, and the con-
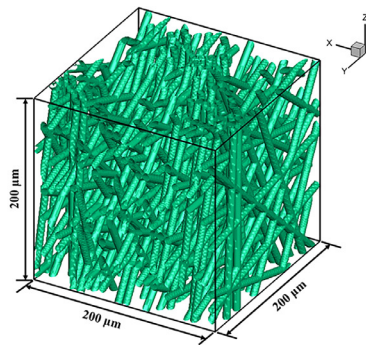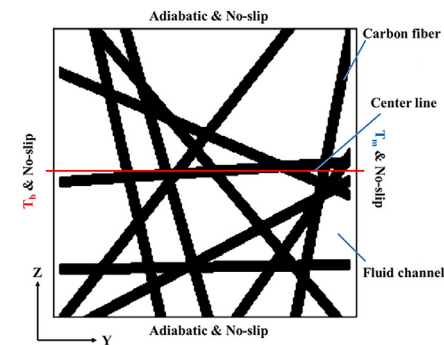

(a) Microstructures of the carbon paper GDL (eg. $\varepsilon_{Overall} = 0.7$)
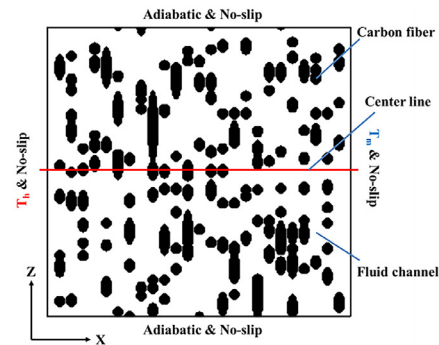
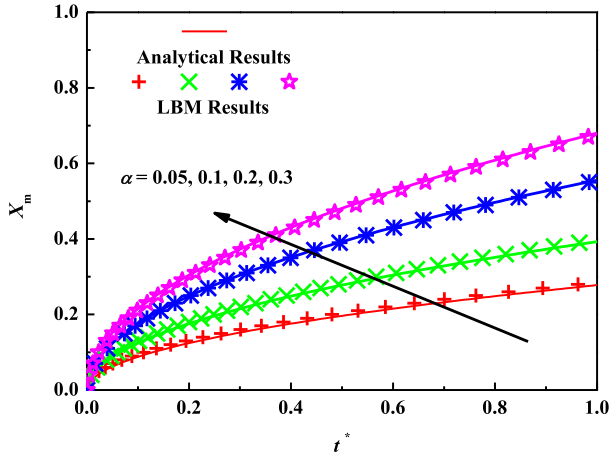(b) Through-plane X position (eg. $\varepsilon_{Through-X} = 0.77$)

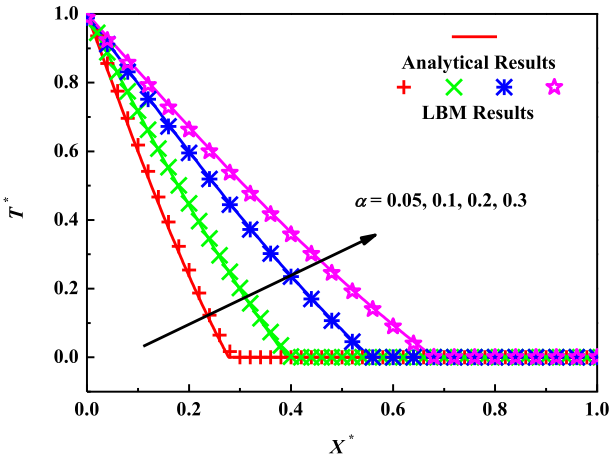(c) Through-plane Z position (eg. $\varepsilon_{Through-Z} = 0.77$)

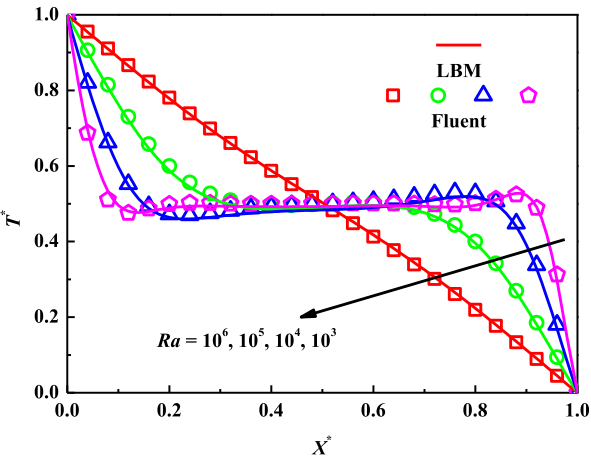(d) In-plane position (eg. $\varepsilon_{In-plane} = 0.69$)

Fig. 3. Computational domain.

(a) Comparison of solid-liquid interface position at different dimensionless time between analytical solution and LBM results for conduction melting.

(b) Comparison of the dimensionless temperature distribution between analytical solutions and LBM results for conduction melting (t^*=1.0).

(c) Comparison of temperature distribution between Fluent results and LBM results for natural convection in a square cavity.

Fig. 4. LBM code validation.

Fig. 5. Time evolution of the melting process in different GDL positions ($\varepsilon_{Overall} = 0.7$).

Fig. 6. Time evolution of the melting process in the In-plane position of GDL under different porosities.
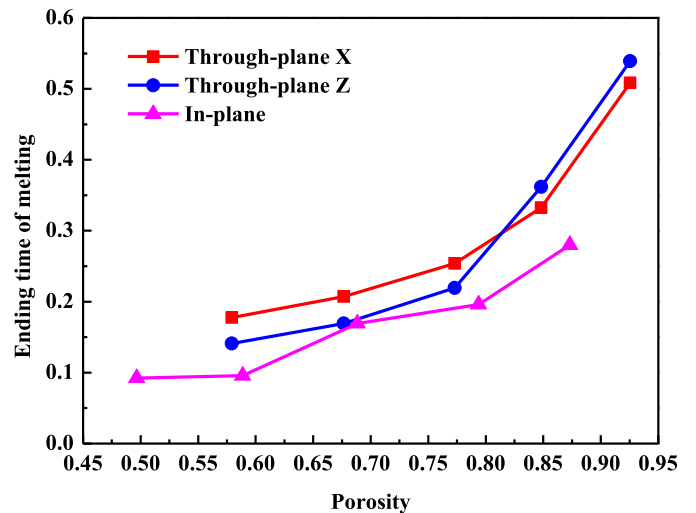
Fig. 7. Effect of porosity on the ending time of melting in different GDL positions.

vection melting is carried out in the GDL. A GDL with complex structure reconstructed by the means of the stochastic algorithm is used in this study. The 3D reconstructed structure of GDL is shown in Fig. 3(a). The carbon paper GDL is consisted of randomly
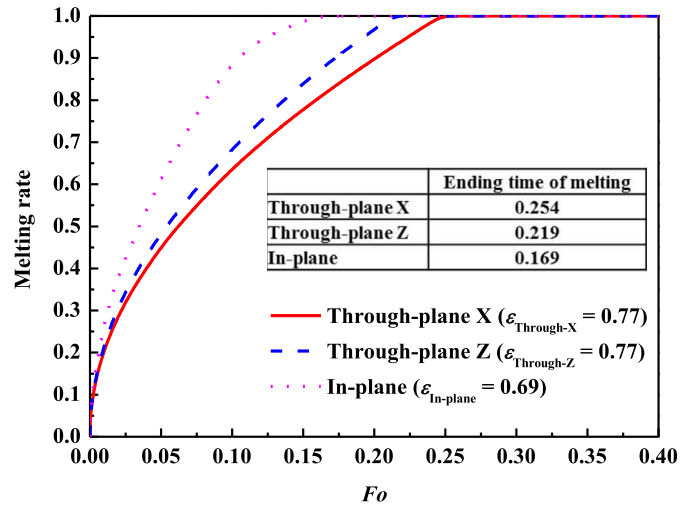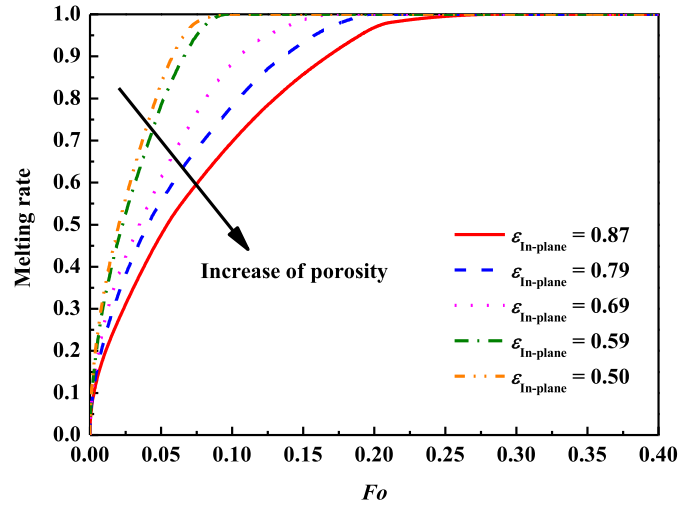
Table 2
Porosities of the reconstructed carbon paper GDL.

Case	Overall porosity	Porosity of cross-section	
		Through-plane X/Z	In-plane
1	0.9	0.9256	0.87
2	0.8	0.8482	0.79
3	0.7	0.7731	0.69
4	0.6	0.67665	0.59
5	0.5	0.57925	0.50

distributed carbon fibers in the In-plane position but layered in the Through-plane position, which resulted in the anisotropy. In this study, the carbon fibers are straight with the fixed diameter and are distributed with random positions and angles in one layer, then, each layer pile up until the porosity satisfies the prescribed porosity. Fig. 3(a) shows a 3D GDL generated with the porosity of 0.7, the fiber diameter of 8 μm and the layer number of 25, and Fig. 3(b) to (d) show the carbon fiber distribution in Through-plane X, Z position and In-plane position on the middle cross-section respectively. The porosities of the cross-section in the Through-plane X, Z and In-plane are 0.77, 0.77 and 0.68 respectively. The boundary condition treatments are described below.

3.5. Boundary conditions

For the LBM boundary of conduction melting without porous structure, as shown in Fig. 1(a), due to the fixed temperature on the left wall, the only one unknown distribution function for the left wall can be achieved by

$$g_1 = T_h - (g_0 + g_2 + g_3 + g_4) \tag{32}$$

For the other three walls, the bounce back boundaries are used.

For the convection melting without porous structure shown in Fig. 1(b), the left wall is set at a high temperature, the right wall is set at melting temperature, and the top and bottom walls are the adiabatic boundaries. All these four walls and carbon fibers are set as no-slip boundaries. For the LBM boundary of heat transfer, due to the fixed temperature of left and right walls, the distribution functions can be computed as

$$g_1 = T_h - (g_0 + g_2 + g_3 + g_4) \tag{33}$$
$$g_3 = T_m - (g_0 + g_1 + g_2 + g_4) \tag{34}$$

Due to the no-slip boundary, the bounce back treatment is used for both walls and carbon particles.

For the problems with porous structures, the boundary conditions are shown in Fig. 3, and numerically they can be treated in the same way presented above.

For the conduction melting, the computational domain is meshed by 100 (in X) × 5 (in Y) grids, and for the convection melting, the computational domain is meshed by 200 × 200 grids. The two meshes have been proved to be grid-independent.

3.6. Validation

The conduction melting without a porous structure is investigated first. Compared with the analytical model, the solid-liquid interface position and temperature distribution obtained in this study agree well with that of the analytical solutions. The effect of different thermal diffusivities has been investigated.

Fig. 4(a) shows the solid-liquid interface position at the different dimensionless time. For four different thermal diffusivities $\alpha=$ 0.05, 0.1, 0.2, 0.3 in lattice unit and Stefan number 1, the variation of solid-liquid interface position agrees well with the results of analytical solution Eq. (4). As shown in Fig. 4(a), the solid-liquid interface position moves sharply at the beginning of the melting
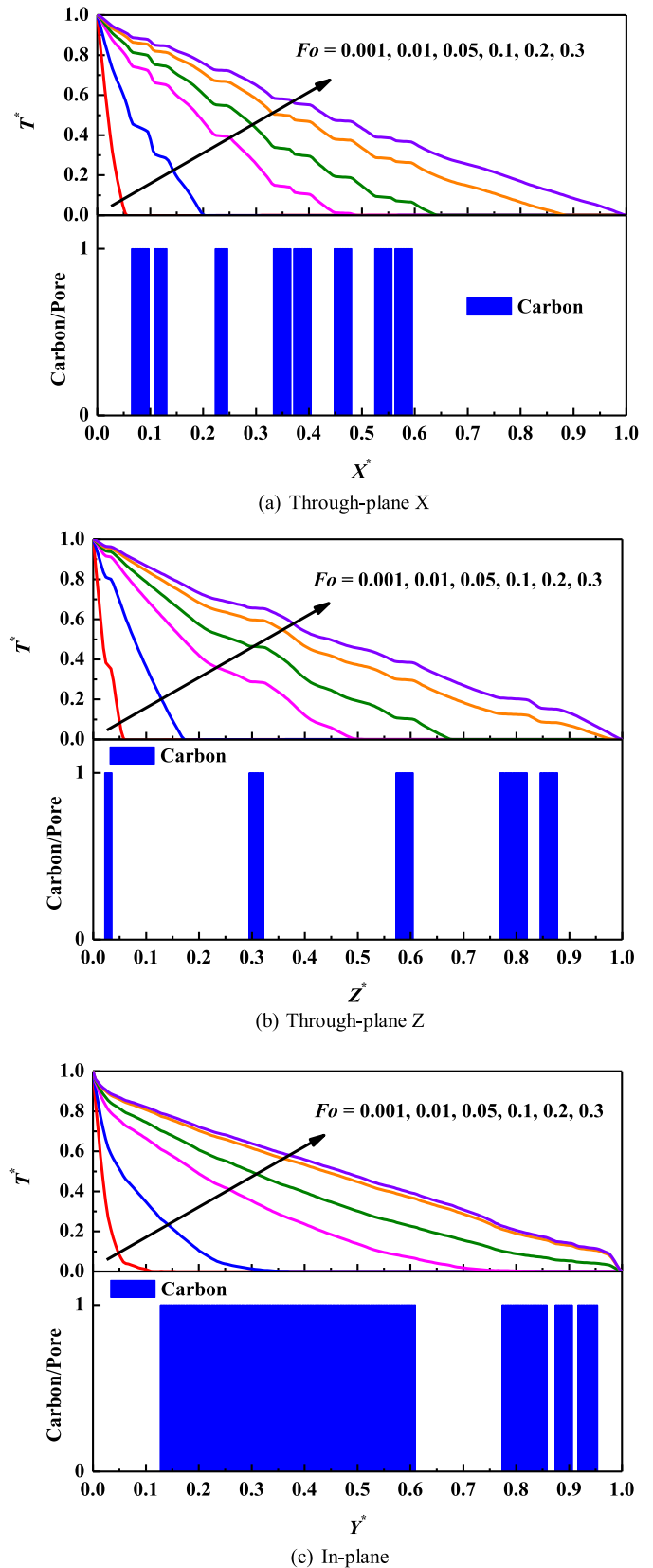

(a) Through-plane X

(b) Through-plane Z

(c) In-plane

Fig. 8. Temperature and carbon fibers distribution on the centerline ($\varepsilon_{Overall} = 0.7$).

process, and with the increasing of time, the variation speed of the solid-liquid interface position decreases. Furthermore, the variation of the solid-liquid interface position becomes fast with the increasing of the thermal diffusivity.
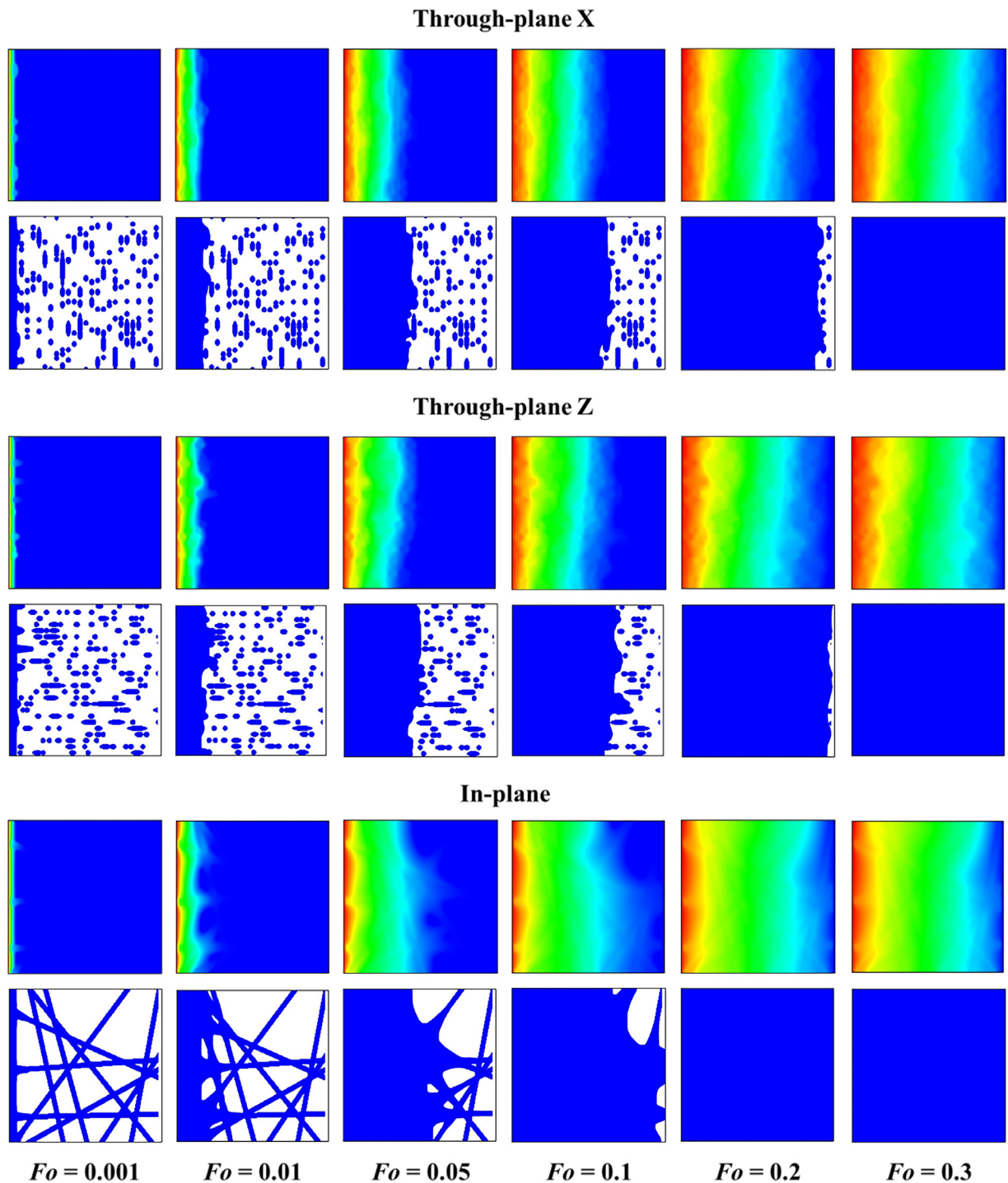
Through-plane X

Through-plane Z

In-plane

$$Fo = 0.001 \qquad Fo = 0.01 \qquad Fo = 0.05 \qquad Fo = 0.1 \qquad Fo = 0.2 \qquad Fo = 0.3$$

Fig. 9. Time evolution of temperature (upper row) and solid-liquid interface (lower row) distribution ($\varepsilon_{\text{Overall}} = 0.7$).

Fig. 4(b) shows the temperature distribution along with X position at different thermal diffusivities when the dimensionless time of 1.0. The temperature distribution results from the LBM model agree well with the analytical solution (Eq. (3)).

Validation of LBM code for natural convection in a cavity without melting was conducted by our LBM code and the temperature distributions are compared with the results from Fluent in Fig. 4(c) for Rayleigh numbers from 10^3 to 10^6. The agreement is very good, showing the reliability of the self-developed LBM code.

4. Results and discussion

The actual process in 3-dimensional in nature. In order to avoid the requirement of huge computer resources while can still obtain useful information, numerical studies are conducted in three 2D planes in the middle of the gas diffusion layer, one is an In-plane and the other two are Through-planes.

In the following, the characteristics of the melting process on different positions of GDL under various porosities are discussed firstly in Section 4.1, then, the effects of Rayleigh number, Stefan
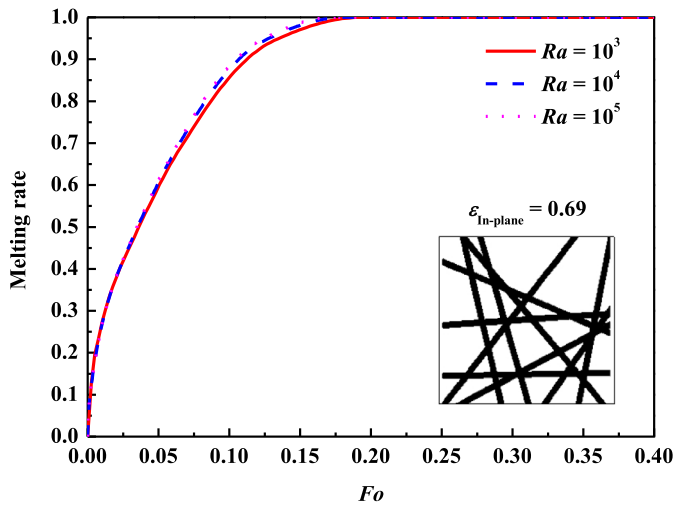
Fig. 10. Time evolution of the melting process in the In-plane position of GDL under different Ra ($\varepsilon_{\text{Overall}} = 0.7$).

number on the melting process and ending time of melting are evaluated in Sections 4.2 and 4.3 respectively.

4.1. Characteristics of melting process in the gas diffusion layer

Due to the anisotropic and porous structure of GDL, the melting process of the ice in pores can be affected by the carbon fibers distribution. During the cold start process of the fuel cell, the ice in the pores of GDL can affect the fuel gas diffusion in porous electrode directly, thus, different overall porosities from 0.9 to 0.5 are investigated, with the Ra and St being fixed as 10^5 and 1.0 respectively, and the porosities of the cross-section in three positions (Through-plane X, Through-plane Z and In-plane) are listed in Table 2.

In order to evaluate the development of the melting process, the melting rate φ is defined as

$$\varphi = \frac{\sum V_{\text{water}}}{V_{\text{pores}}} \tag{35}$$

where V_{water} is the volume of water which is produced during the phase change process, V_{pores} is the total volume of the pores. The melting rate shows the melting process of ice in the pores of GDL. When the pores of GDL are filled up with ice, the melting rate equals 0. During the melting process, the melting rate verifies from 0 to 1.0. When the ice all melts into water, the melting rate equals 1.0.

As shown in Fig. 5, the GDL section positions have a significant effect on the melting process, and the melting process in different positions has a different melting rate, which is mainly caused by the carbon fibers distribution. It should be noted that the ending time is dimensionless (Fourier number). Comparing the change of melting rate, the melting rate in the In-plane position increases fastest among the three positions, while the Through-plane X position increases the lowest, and the Through-plane Z position is in between. In addition, the ending time of melting is used to quantitatively evaluate the melting process, which is defined as the time when the ice in pores is all melted. Among the three positions, the ending time of melting in the In-plane position is the shortest, which is only 0.169, while the Through-plane X is the longest, which is 0.254, and the Through-plane Z is in between (0.219). Compared with the Through-plane, the ice in the In-plane position melts fastest. This is mainly caused by two reasons, on the one hand, the porosity in In-plane position is the smallest, and the high thermal conductivity of carbon fibers allow the temperature
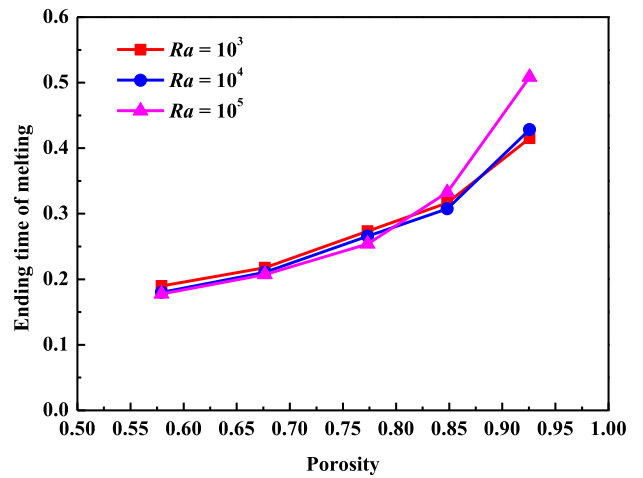
(a) Through-plane X
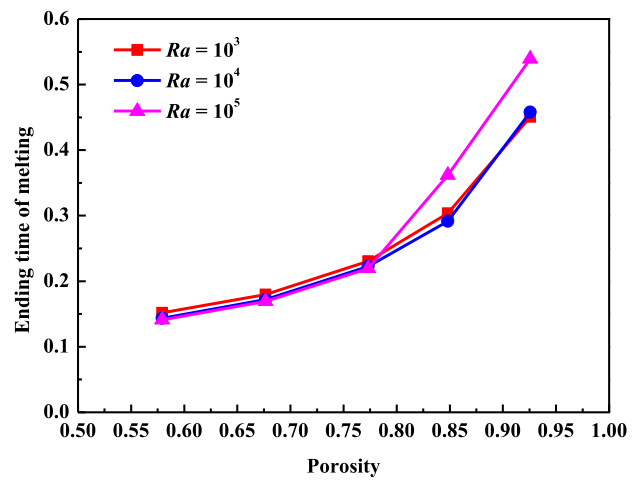
(b) Through-plane Z
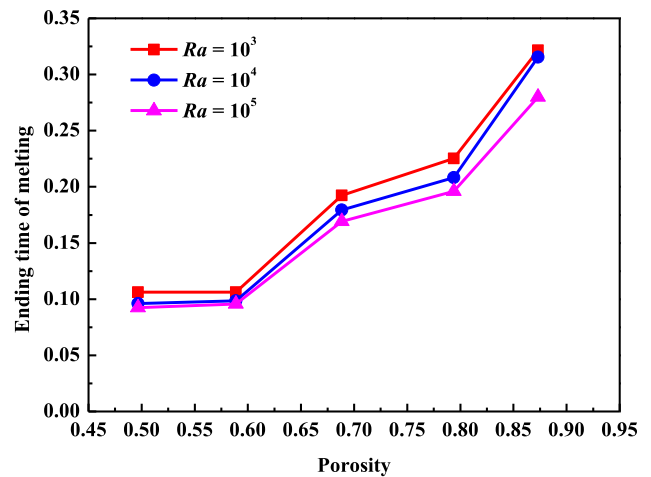
(c) In-plane

Fig. 11. Effect of Ra on the ending time of melting in different GDL positions.

to be quickly transmitted, which can speed up the melting process, on the other hand, in the In-plane position a number of continuous fibers exist as shown in Fig. 3(d) which have higher thermal conductivity and finally accelerates the ice melting. Comparing the melting process in the X and Z positions of the Through-plane, the Z position is faster than the X position, which is mainly due

to the influence of the carbon fiber distribution anisotropy. In the Through-plane position, the carbon fiber in the Z position is longer than that of X position, leading to more long-cross sections in Through-plane Z position (Fig. 3(c)) than that in Through-plane X position (Fig. 3(b)) which can cause the melting rate in the Z position to be faster than X position.

In order to evaluate the effect of porosity on the melting process, Fig. 6 shows the variation of melting rate with dimensionless time under different porosities in the In-plane position. With the increase in porosity, the melting rate decreases. Thus, reducing the porosity can effectively promote the melting process of ice.

Fig. 7 shows the change of ending time of melting with the porosity in three positions of GDL. From the figure, two features may be noted. First, the ending time increases with the increase in porosity, and the ending time in the In-plane position is the smallest in all the cases. Second, when the porosity is greater than 0.83, the ending time in the Through-plane Z position is longer than that of the Through-plane X position, while when the porosity is less than 0.83 the ending time in the Through-plane Z position is shorter than Through-plane X position.

Fig. 8 shows the temperature and carbon fiber distribution on the centerline (shown as Fig. 3) of the GDL in three positions. Comparing Fig. 8(a) to (c), it can be seen that the ice melting process in the In-plane position on the centerline completes earliest, followed by the Through-plane Z position, and finally the Through-plane X position, which is consistent with the discussion above. In addition, there exists a significant temperature gradient change between carbon fibers and pores, which is mainly caused by the difference in thermal conductivity of carbon fibers and pores.

Fig. 9 shows the time evolution of temperature and solid-liquid interface distribution in three positions of GDL. As shown in Fig. 9, the distribution of carbon fibers has a significant effect on the heat transfer and evolution of the solid-liquid interface, especially in the results of the In-plane position. Comparing to the temperature distribution evolution in the In-plane and the two Through-plane positions, the distribution of carbon fibers in the In-plane position is more favorable for the temperature uniformity than the Through-plane position.

4.2. Effect of Rayleigh number

The cases with Rayleigh numbers ranging from 10^3 to 10^5 are investigated. In this section, the Stefan number is fixed as 1.0, the overall porosity of GDL ranges from 0.9 to 0.5, and the melting process in the Through-plane X, Through-plane Z and In-plane positions are evaluated.

Fig. 10 shows the effect of different Rayleigh numbers on the melting process in the In-plane position. The results show that at beginning stage ($Fo < 0.05$) the increase of natural convection intensity from $Ra = 10^3$ to 10^5 has no effect on the melting rate, and after that point, a minor difference can be found between the three Rayleigh numbers, with a larger Ra having a bit quicker melting rate. However, as a whole within $Ra = 10^3$ to 10^5 the Rayleigh number effect is not significant.

Fig. 11 shows the change of the ending time of melting in three positions of GDL with porosity under different Rayleigh numbers. For the melting process in the Through-plane X position, when the porosity is larger than 0.85, the low Rayleigh number is beneficial to the completion of the melting process (as shown in Fig. 11(a)). This is mainly caused by the following fact. When the porosity is large, the pores in GDL are also large, which is conducive to the occurrence of natural convection, resulting in areas that are not easily melted in the lower right corner, which finally hinders the process of melting in the whole region. On the other hand, when the porosity is smaller than 0.85 the Rayleigh number has no significant effect on the melting process. This is mainly because when
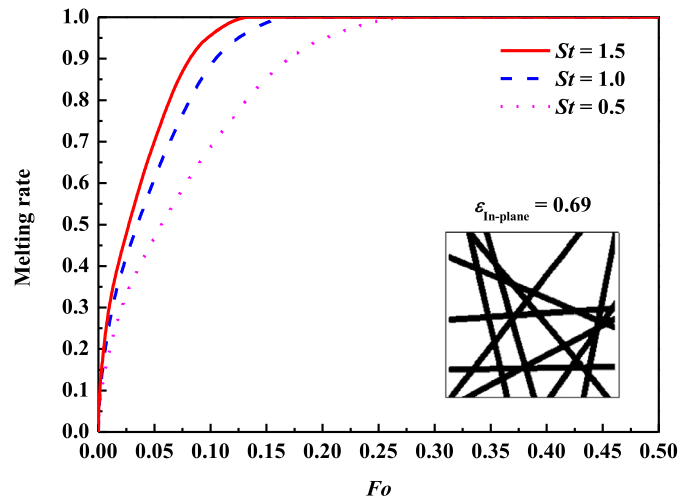

Fig. 12. Time evolution of the melting process in the In-plane position of GDL under different *St*.
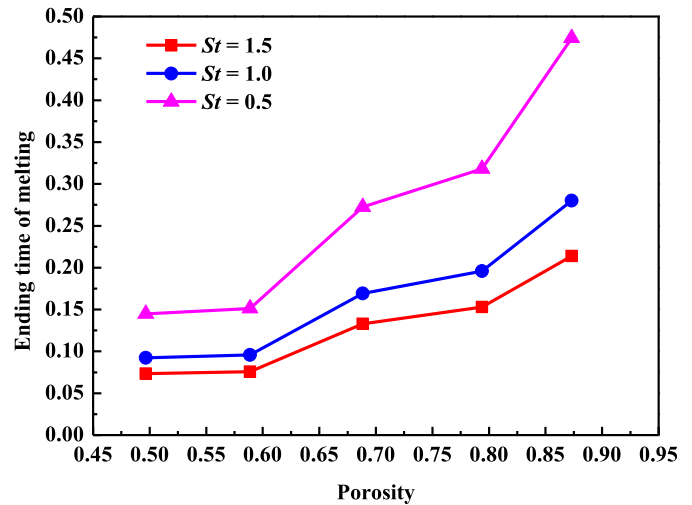

Fig. 13. Effect of *St* on the ending time of melting under different porosities in the In-plane position.

the porosity is small the natural convection can not be easily developed, and the heat transfer is actually dominated by conduction mechanism. Comparing with the Through-plane X position, the Rayleigh number has a similar effect on the melting process, but when the turning porosity is 0.78 (Fig. 11(b)). This suggests that the position of carbon fiber has an effect on the degree of natural convection. The results of In-plane (Fig. 11(c)) show that within the entire porosity range higher Rayleigh number is in favor of enhancing heat transfer with the effect being more obvious with the increase in porosity. This is mainly caused by the reason that the big pores contribute to the occurrence of natural convection, which is helpful to the enhancement of heat transfer process and accelerates the melting of ice.

4.3. Effect of Stefan number

As defined by Eq. (5b), Stefan number is a ratio of sensitive heat over latent heat. In order to study its effect on the melting process, three different Stefan numbers are investigated, which are 0.5, 1.0 and 1.5 respectively. In this section, the Rayleigh number is fixed as 10^5, and the melting process in the In-plane position is studied.

Fig. 12 shows the effect of Stefan numbers on the melting process in the In-plane position. It can be seen that the increase of

Stefan number can promote the melting process significantly, especially at the lower Stefan number range. This is consistent with the physical meaning of Stefan number: the decrease in Stefan number implies the deduction of latent heat, hence the melting process can be enhanced.

Fig. 13 shows the effect of Stefan number on the ending time of melting under different porosities. It can be seen that the variation trend is the same as St vs melting rate. And the same reason explained above can also be applied.

Finally its worthing noting that the transport in the GDL is 3D in nature. In this paper as the firsts stage for reveaing the major features of diffusion process in the two important directions, the process is decoupled into In-plane and Through-plane simulations. The 3D simulations are now underway and will be presented elsewhere in the furthure.

5. Conclusions

In this study, a 2D lattice Boltzmann model combining the enthalpy-based method (EBM) is established to investigate the ice melting process in the gas diffusion layer (GDL). The effects of GDL melting position, porosity, Rayleigh number and Stefan number on the melting rate, ending time of melting, temperature distribution and solid-liquid interface distribution are investigated. The main conclusions can be derived as follows:

1 The GDL melting positions have a significant effect on the melting process, the melting process in the In-plane position is the fastest compared with the Through-plane X and Through-plane Z positions.
2 When the porosity is large, the effect of carbon fiber layer number on the melting process is more significant than that of fiber length, but when the porosity is small, the carbon fiber length has a more significant influence on the melting process.
3 Reducing the GDL porosity can effectively promote the melting process of ice.
4 In the In-plane position, the increase of natural convection intensity has a promoting effect on the ice melting process when Ra increases from 10^3 to 10^4, and a further increase in Ra from 10^4 to 10^5, the promotion effect becomes less significant.
5 In the Through-plane positions, a large porosity hinders the process of melting in the whole region.
6 The increase of Stefan number can promote the melting process significantly, and its effect becomes weaker with a further increase in Stefan number.

Declaration of Competing Interest

We declare that we have no conflict of interest.

CRediT authorship contribution statement

Pu He: Conceptualization, Methodology, Software, Validation, Formal analysis, Investigation, Resources, Writing - original draft. **Li Chen:** Methodology, Funding acquisition. **Yu-Tong Mu:** Methodology, Funding acquisition. **Wen-Quan Tao:** Writing - review & editing, Visualization, Supervision, Project administration, Funding acquisition.

Acknowledgments

Supplementary materials

References

[1] M. Jourabian, M. Farhadi, A.A.R. Darzi, Outward melting of ice enhanced by Cu nanoparticles inside cylindrical horizontal annulus: lattice Boltzmann approach, Appl. Math. Model. 37 (2013) 8813–8825.
[2] Z. Chen, D. Gao, J. Shi, Experimental and numerical study on melting of phase change materials in metal foams at pore scale, Int. J. Heat Mass Transf. 72 (2014) 646–655.
[3] M. Jourabian, M. Farhadi, K. Sedighi, On the expedited melting of phase change material (PCM) through dispersion of nanoparticles in the thermal storage unit, Comput. Math. Appl. 67 (2014) 1358–1372.
[4] R. Hossai, S. Mahmud, A. Dutta, I. Pop, Energy storage system based on nanoparticle-enhanced phase change material inside porous medium, Int. J. Therm. Sci. 91 (2015) 49–58.
[5] Q. Yan, H. Toghiani, Y. Lee, K. Liang, H. Causey, Effect of sub-freezing temperatures on a PEM fuel cell performance, startup and fuel cell components, J. Power Sources 160 (2006) 1242–1250.
[6] K. Tajiri, Y. Tabuchi, C.Y. Wang, Isothermal cold start of polymer electrolyte fuel cells, J. Electrochem. Soc. 154 (2) (2007) B147–B152.
[7] K. Jiao, X. Li, Effects of various operating and initial conditions on cold start performance of polymer electrolyte membrane fuel cells, Int. J. Hydrog. Energy 34 (2009) 8171–8184.
[8] K. Jiao, I.E. Alaefour, G. Karimi, X. Li, Cold start characteristics of proton exchange membrane fuel cells, Int. J. Hydrog. Energy 36 (2011) 11832–11845.
[9] A. Abhat, Low temperature latent heat thermal energy storage: heat storage materials, Sol. Energy 30 (4) (1981) 313–332.
[10] J. Prakash, H.P. Garg, G. Datta, A solar water heater with a built-in latent heat storage, Energy Convers. Manage. 25 (1) (1985) 51–56.
[11] E.B.S. Mettawee, G.M.R. Assassa, Experimental study of a compact PCM solar collector, Energy 31 (2006) 2958–2968.
[12] A. Sharma, V.V. Tyagi, C.R. Chen, D. Buddhi, Review on thermal energy storage with phase change materials and applications, Renew. Sustain. Energy Rev. 13 (2009) 318–345.
[13] C.J. Ho, J.Y. Gao, Preparation and thermo-physical properties of nanoparticle-in-paraffin emulsion as phase change material, Int. Commun. Heat Mass Transf. 36 (5) (2009) 467–470.
[14] J.M. Khodadadi, S.F. Hosseinizadeh, Nanoparticle-enhanced phase change materials (NEPCM) with great potential for improved thermal energy storage, Int. Commun. Heat Mass Transf. 34 (2007) 534–543.
[15] H.H. Al-Kayiem, S.C. Lin, Performance evaluation of a solar water heater integrated with a PCM nanocomposite TES at various inclinations, Sol. Energy 109 (2014) 82–92.
[16] R.K. Ahluwalia, X. Wang, Rapid self-start of polymer electrolyte fuel cell stacks from subfreezing temperatures, J. Power Sources 162 (2006) 502–512.
[17] H. Meng, Numerical analyses of non-isothermal self-start behaviors of PEM fuel cells from subfreezing startup temperatures, Int. J. Hydrog. Energy 33 (2008) 5738–5747.
[18] K. Jiao, X. Li, Three-dimensional multiphase modeling of cold start processes in polymer electrolyte membrane fuel cells, Electrochim. Acta 54 (2009) 6876–6891.
[19] Q. Guo, Y. Luo, K. Jiao, Modeling of assisted cold start processes with anode catalytic hydrogen-oxygen reaction in proton exchange membrane fuel cell, Int. J. Hydrog. Energy 38 (2013) 1004–1015.
[20] Q. Du, B. Jia, Y. Luo, J. Chen, Y. Zhou, K. Jiao, Maximum power cold start mode of proton exchange membrane fuel cell, Int. J. Hydrog. Energy 39 (2014) 8390–8400.
[21] Y. Mu, P. He, J. Ding, W.Q. Tao, Modeling of the operation conditions on the gas purging performance of polymer electrolyte membrane fuel cells, Int. J. Hydrog. Energy 42 (2017) 11788–11802.
[22] L. Chen, Q. Kang, Y.L. He, W.Q. Tao, Pore-scale simulation of coupled multiple physicochemical thermal processes in micro reactor for hydrogen production using lattice Boltzmann method, Int. J. Hydrog. Energy 37 (2012) 13943–13957.
[23] L. Chen, Q. Kang, B.A. Robinson, Y.L. He, W.Q. Tao, Pore-scale modeling of multiphase reactive transport with phase transitions and dissolution-precipitation processes in closed systems, Phys. Rev. E 87 (2013) 043306.
[24] L. Chen, Q. Kang, B. Carey, W.Q. Tao, Pore-scale study of diffusion-reaction processes involving dissolution and precipitation using the lattice Boltzmann method, Int. J. Heat Mass Transf. 75 (2014) 483–496.
[25] L. Chen, Q. Kang, Y. Mu, Y.L. He, W.Q. Tao, A critical review of the pseudopotential multiphase lattice Boltzmann model: Methods and applications, Int. J. Heat Mass Transf. 76 (2014) 210–236.
[26] L. Chen, H.B. Luan, Y.L. He, W.Q. Tao, Pore-scale flow and mass transport in gas diffusion layer of proton exchange membrane fuel cell with interdigitated flow field, Int. J. Therm. Sci. 51 (2012) 132–144.
[27] L. Chen, G. Wu, E.F. Holby, P. Zelenay, W.Q. Tao, Q. Kang, Lattice Boltzmann pore-scale investigation of coupled physical-electrochemical processes in C/Pt and non-precious metal cathode catalyst layers in proton exchange membrane fuel cells, Electrochim. Acta 158 (2015) 175–186.

[28] L. Chen, R. Zhang, P. He, Q. Kang, Y.L. He, W.Q. Tao, Nanoscale simulation of local gas transport in catalyst layers of proton exchange membrane fuel cells, Power Sources 400 (2018) 114–125.

[29] Y. Mu, Adam Z. Weber, Zhao-Lin Gu, W.Q. Tao, Mesoscopic modeling of transport resistances in a polymer-electrolyte fuel-cell catalyst layer: Analysis of hydrogen limiting currents, Appl. Energy 255 (2019) 113895.

[30] W.S. Jiaung, J.R. Ho, C.P. Kuo, Lattice Boltzmann method for the heat conduction problem with phase change, Numer. Heat Transf. Part B 39 (2001) 167–187.

[31] D. Chatterjee, S. Chakraborty, An enthalpy-based lattice Boltzmann model for diffusion dominated solid–liquid phase transformation, Phys. Lett. A 341 (2005) 320–330.

[32] C. Huber, A. Parmigiani, B. Chopard, M. Manga, O. Bachmann, Lattice Boltzmann model for melting with natural convection, Int. J. Heat Fluid Flow 29 (2008) 1469–1480.

[33] Z. Li, M. Yang, Y. Zhang, Numerical simulation of melting problems using the lattice Boltzmann method with the interfacial tracking method, Numer. Heat Transf. Part A 68 (2015) 1175–1197.

[34] Z. Li, M. Yang, Y. Zhang, Lattice Boltzmann method simulation of 3-D natural convection with double MRT model, Int. J. Heat Mass Transf. 94 (2016) 222–238.

[35] B. Šarler, Stefan's work on solid-liquid phase changes, Eng. Anal. Bound. Elem. 16 (1995) 83–92.

[36] E. Bodenschatz, W. Pesch, G. Ahlers, Recent developments in Rayleigh-Bénard convection, Annu. Rev. Fluid Mech. 32 (2000) 709–778.

[37] S.Y. Chen, G.D. Doolen, Lattice Boltzmann method for fluid flows, Annu. Rev. Fluid Mech. 30 (1998) 329–364.

[38] S.P. Sullivan, F.M. Sani, M.L. Johns, L.F. Gladden, Simulation of packed bed reactors using lattice Boltzmann methods, Chem. Eng. Sci. 60 (2005) 3405–3418.

[39] W.S. Jiaung, J.R. Ho, C.P. Kuo, Lattice-Boltzmann method for the heat conduction problem with phase change, Numer. Heat Transf. Part B 39 (2) (2001) 167–187.